



OPEN

DATA DESCRIPTOR

High throughput calculations for a dataset of bilayer materials

Ranjan Kumar Barik[✉] & Lilia M. Woods[✉]

Bilayer materials made of 2D monolayers are emerging as new systems creating diverse opportunities for basic research and applications in optoelectronics, thermoelectrics, and topological science among others. Herein, we present a computational bilayer materials dataset containing 760 structures with their structural, electronic, and transport properties. Different stacking patterns of each bilayer have been framed by analyzing their monolayer symmetries. Density functional theory calculations including van der Waals interactions are carried out for each stacking pattern to evaluate the corresponding ground states, which are correctly identified for experimentally synthesized transition metal dichalcogenides, graphene, boron nitride, and silicene. Binding energies and interlayer charge transfer are evaluated to analyze the interlayer coupling strength. Our dataset can be used for materials screening and data-assisted modeling for desired thermoelectric or optoelectronic applications.

Background & Summary

Monolayered materials have attracted considerable research interest in science and technology due to their inherent novel properties compared to their bulk counterparts. Systems, such as transition metal dichalcogenides (TMDs)¹, Janus monolayers², MXene³, boron nitride (BN)⁴, phosphorene⁵, and others⁶, have proven as excellent candidates for thermoelectrics⁷, optoelectronics⁸, and spintronics⁹ nanoscale device applications. Starting with graphene¹⁰, layered materials and their heterostructures have been the source of emergent phenomena coupling their electronic, optical, thermal, and mechanical response with nontrivial topology. For example, hexagonal honeycomb materials can host valley Hall effect and quantum anomalous Hall effect providing a platform to study dissipation-less valleytronics¹¹. Layered materials with broken inversion symmetry could lead to *k*-valley-dependent contrasted circular dichroism, enabling valley optical selection rules¹². Different substrate environments can provide substantial Rashba effect, making it possible to design spintronics devices such as spin-field effect transistors¹³.

Layered materials are typically composed of chemically inert monolayers that can be organized to make various multilayer composites. In addition to individual layers, systems that consist of finite number of identical monolayers or heterostructures made of layers with different chemical compositions give rise to new subfields in science and technology. The diversity is practically limitless given the ever increasing library of layered materials^{14,15}. Recent large scale simulations predict over 4000 2D materials with different chemical compositions and lattice space groups¹⁶. Some of them have been synthesized such as transition metal dichalcogenides (TMDs)¹⁷, hexagonal boron nitride (hBN)¹⁸, graphene¹⁹, MSe₂ (M = Zr, Hf)^{20,21}, ZrS₂²², TiS₂²³, MoSSe²⁴ and so on, while others are waiting to be realized in the laboratory.

In addition to their monolayer phase, bilayers constitute a separate subset of 2D materials whose different stacking patterns and interlayer interactions become additional sources of new physics^{25,26}. In particular, the semimetallic behavior of graphene limits its application in the next-generation device application; however, its bilayer has a tunable band gap via external electric fields, enabling its device applications²⁷. On the other hand, various types of stacking patterns in bilayers could offer a platform to study different novel phenomena, including magneto-electric coupled multiferroics effect²⁸, different optical response^{29,30}, topology³¹, magnetism³², and Rashba spin-splitting³³. Besides, different twisting angles of monolayers can exhibit moiré patterns resulting in many intriguing properties, such as Mott insulating behavior³⁴, topological superconducting state³⁵, tunable band gaps³⁶, and light-matter interactions³⁷ providing an opportunity to study twistronics in a large class of bilayers.

Department of Physics, University of South Florida, Tampa, Florida, 33620, USA. ✉e-mail: rran9125@gmail.com; lmwoods@usf.edu

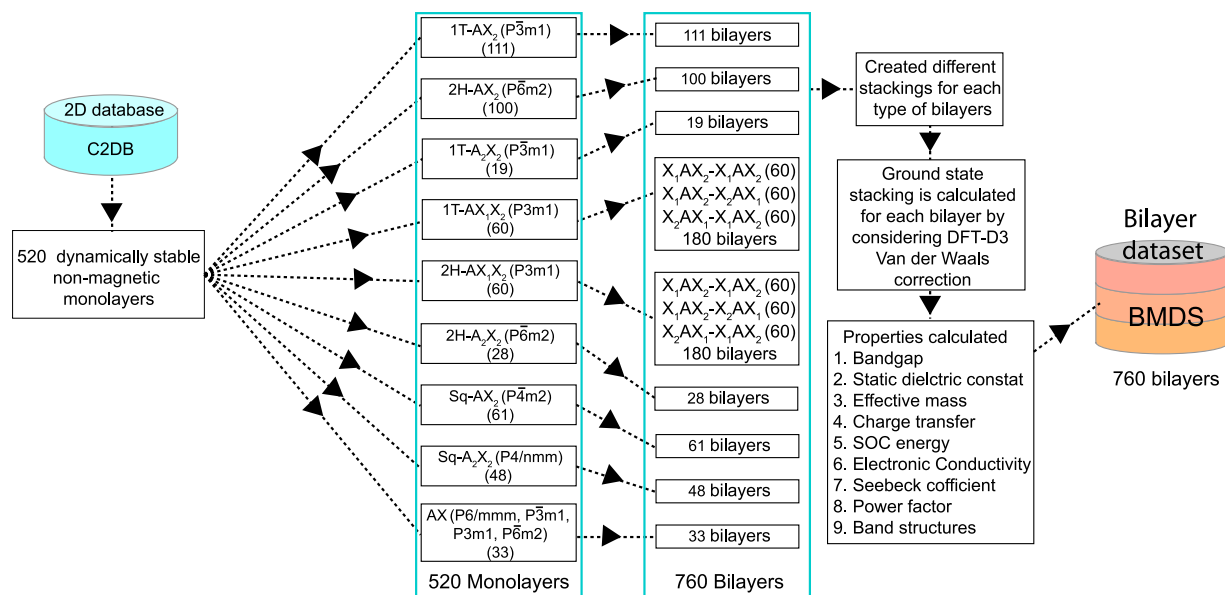


Fig. 1 High through-put work flow for building the bilayer materials dataset (BMDS), where the symmetries of 520 dynamically stable nonmagnetic 2D structures are analyzed to construct and simulate bilayers made of identical monolayers using the DFT methods.

In this study, we report high throughput Density Functional Theory (DFT) calculations of van der Waals bilayer materials, composed of chemically inert dynamically stable nonmagnetic monolayers as reported in the C2DB database site¹⁶. We consider monolayers with hexagonal and square type lattices with various stackings obtained by rotating or sliding the top layer against the bottom layer as dictated by the symmetry of each monolayer. Besides, many of the different stacking patterns can be viewed as variations of the AA and AB bilayer orientations for bilayer graphene³⁸. For each of the constructed 760 bilayers, the energetically most stable configuration is reported together with several electronic and transport properties. By calculating the density of states (DOS) and band structures, energy gaps in the $0 \leq E_g < 6$ eV are found, further highlighting the role of spin orbit coupling (SOC). Lattice parameters, interlayer separations, van der Waals coupling, and charge transfer are also calculated to generate data driven information of interlayer effects in bilayers. Additionally, calculated Seebeck coefficient, electrical conductivity, and effective band structure masses provide the foundation for a transport database³⁹ properties of 2D materials. The reported data gives valuable information for screening and identifying materials with targeted properties as well as a set of descriptors to be used in future statistical models based on data mining and machine learning methods^{40,41}.

Methods

Work flow. The high throughput computational work flow to build the bilayer materials dataset is shown in Fig. 1. The initial set of materials is taken from the C2DB database⁴², where we consider non-magnetic and dynamically stable monolayers for further screening. The breakdown of the stoichiometry, group symmetry, and the corresponding number of monolayers are also given explicitly. A total of 520 monolayers have been examined and schematic representation of those monolayers is provided in Fig. S1 with their lattice constants given in Fig. S2 of the Supporting Information.

The symmetries in each monolayer type have been analyzed to generate different bilayer stacking patterns having chemically identical monolayers. These stacking patterns are created by considering an initial interlayer separation of 3.3 Å. Besides the atomic registry dependence, the different surface atoms in the Janus (AX_1X_2) 1T and 2H phases have provided additional adaptability for constructing the Janus-derived bilayers. We framed three distinct bilayers phases as X_1AX_2 - X_2AX_1 (60 structures), X_1AX_2 - X_1AX_2 (60 structures), and X_2AX_1 - X_1AX_2 (60 structures) with X_2 - X_2 , X_2 - X_1 , and X_1 - X_1 atoms making up the interface region. Accordingly, 760 bilayers with nine different phases have been formulated from the initial 520 monolayers.

DFT self-consistent calculations are then performed by considering the van der Waals interactions to obtain the relaxed structures of all bilayers. Energies of the stackings in each bilayer type are compared, and the stacking order of the energetically most stable system is identified as the ground state configuration for our bilayer materials dataset (BMDS). Subsequently, electronic structure calculations are carried out to obtain the energy band gaps with and without SOC, the magnitude of the SOC energy, charge transfer between the layers, effective masses at the valence band maxima and conduction band minima of the most stable bilayers. These results are reported in the BMDS. Transport properties, such as the scaled electrical conductivity (σ/τ), Seebeck coefficient (S), and scaled Power factor ($S^2\sigma/\tau$) within a constant relaxation time approximations τ are also calculated. These data are also provided in our BMDS dataset⁴³.

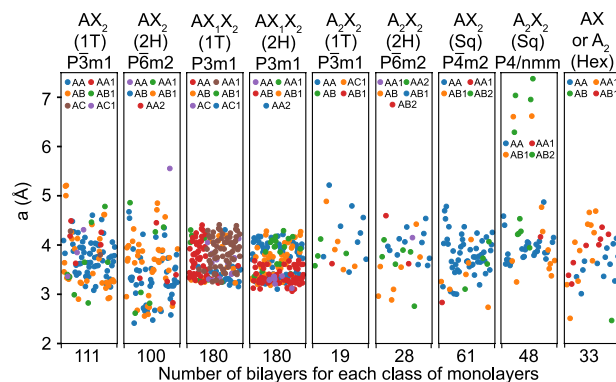


Fig. 2 Lattice parameters for bilayers formed from different classes of monolayers. The scattered plots contain the data for most energetically stable stacking order for each material represented by a distinct color dot.

Detailed computational calculations and reported materials properties are discussed in what follows.

Materials design and density functional theory calculations. The construction of the differently stacked bilayers is facilitated by analyzing the crystal symmetries of the constituent monolayers^{44–50}, which is implemented by using combinations of different slidings and/or 180° rotations of the hexagons or squares making up the monolayer lattices. The atomic representation of the stacking patterns with a convenient notation of each class of materials is given in Figs. S3–S12 in the Supporting Information. The centrosymmetric AX_2 and A_2X_2 hexagonal systems with three and four atoms in the unit cell and the non-centrosymmetric Janus monolayers AX_1X_2 have six possible bilayer stacking patterns. The square monolayers in AX_2 and A_2X_2 stoichiometries with three or four unit cells have four distinct bilayer stacking patterns. The configurations of monolayers with two atoms per unit cell depend upon the presence of finite thickness, such that planar materials (such as graphene) have two stacking patterns while finite thick materials have four possible stacking patterns.

The stacking configurations for the considered bilayers are calculated using DFT methods as implemented in the Vienna Ab initio Simulation Package (VASP)⁵¹. The projector-augmented wave (PAW) potentials are used to incorporate the ion-electron interactions in the calculations⁵². The Perdew-Burke-Ernzerhof (PBE) functional within the generalized gradient approximation is adopted to estimate the exchange-correlation potential⁵³. To expand the wavefunctions on a plane-wave basis, a kinetic energy cutoff of 600 eV is used with an energy convergence threshold of 10^{-6} eV. The structures were relaxed by utilizing a conjugate gradient scheme until each component of Hellmann-Feynman forces on the atoms was less than $0.005 \text{ eV}\text{\AA}^{-1}$. A Γ -centered $12 \times 12 \times 1$ Monkhorst-Pack⁵⁴ k-point grid is considered for sampling the Brillouin Zone. A minimum vacuum layer of 15 Å is taken to avoid interactions with adjacent layers. Electronic band structure and transport properties are calculated by considering the SOC effect. The charge difference between the monolayer and bilayer has been calculated by Bader charge analysis⁵⁵. The van der Waals interaction in different stacking is approximated by considering the DFT-D3 method with a zero-damping function⁵⁶. Effective masses of VBM and CBM are calculated using the SUMO PYTHON package⁵⁷.

Structural, electronic, and dielectric properties of bilayer materials. All the data presented here concerns the ground state for each bilayer, which is identified by comparing the total energies as found from DFT and selecting the minimum value

$$E = \min \{E_1, E_2, \dots, E_n\} \quad (1)$$

where E_1, E_2, \dots, E_n are the total DFT energies for all n possible stacking patterns of a given bilayer, as explicitly given in Figs. S3–S12 in the Supporting Information. Scattered plots of the lattice constant a and interlayer separation d in terms of number of materials for all nine bilayer sub-classes are shown in Figs. 2, 3, respectively, where each ground state is represented by a distinct color dot. The stoichiometry and space group belonging to their respective monolayer constituents are also denoted. In the CSV spreadsheet, we show a full list of both lattice constants a and d , which can further be compared with the lattice constants a of the monolayers given in Fig. S2 in the Supporting Information. Although many bilayers are found to be anisotropic, the difference between the a and b lattice constants is rather small. In most bilayers, a lies within 3–4.5 Å, and this trend is especially pronounced for the 1 T and 2 H Janus (AX_1X_2) materials where all data is concentrated in that region. We find that six materials, K_2Br_2 , K_2Cl_2 , K_2I_2 , Rb_2Br_2 , Rb_2Cl_2 , and Rb_2I_2 , in the square lattice phase A_2X_2 (P4/nmm), have much larger bilayer parameters which is consistent with the data for the corresponding monolayers (monolayer lattice parameters are mentioned in Figure S2 in the Supplementary Information).

The numerical data for the interlayer distance d as obtained from DFT is also given in the CSV spreadsheet. For the large majority of systems $d > 2.65$ Å, which implies that chemical effects are relatively small and the bilayer may be considered as van der Waals systems. Nevertheless, several bilayers, especially some that are formed by hexagonal and square AX_2 and square A_2X_2 monolayers have $d < 2.65$ Å indicating that stronger interlayer interactions might be present.

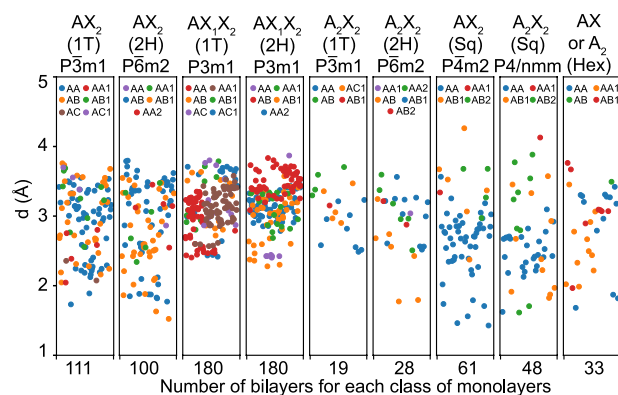


Fig. 3 Interlayer distances for bilayers formed from different classes of monolayers. The scattered plots give data for the most energetically stable stacking order for each material. The calculations include van der Waals corrections.

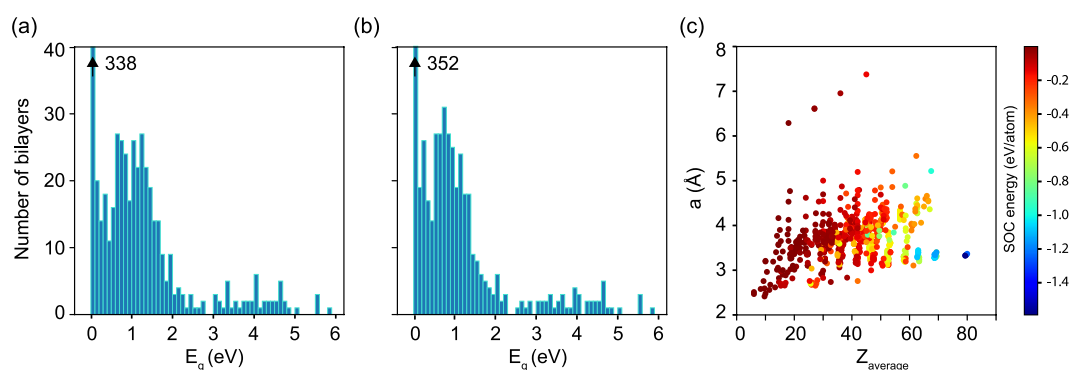


Fig. 4 Histogram plot of the band gaps of all bilayers showing number of materials without (a) and with (b) the SOC effect; (c) scattered plot of the lattice parameter as a function the average atomic number ($Z_{\text{average}} = \frac{\sum_{i=1}^N n_i Z_i}{\sum_{i=1}^N n_i}$, where n_i is the number of i th atom having atomic number Z_i present in the unit cell and N is total number of atomic species) of the bilayers. The dot color (color bar shown to the right of the panel) corresponds to the strength of the SOC energy per atom. All data are for the most stable bilayers configurations with included van der Waals interactions.

After the energetically most stable bilayer configuration for each bilayer is identified based on Eq. 1, the DFT electronic band structure is calculated. The energy band gaps E_g are extracted from these results and grouped in a 0.1 eV intervals for each bilayer type. The data is then plotted in Fig. 4 by a histogram representation for the data without (panel (a)) and with SOC (panel (b)). Since the calculations are done with standard semi-local functionals, which frequently underestimate the energy gaps, it is possible that for some materials E_g may differ from the ones given here. Nevertheless, our results are consistent with the level of DFT calculations in the monolayer C2DB database^{16,42}. They can also provide a good idea about the metallic-semiconducting-insulating properties of bilayer materials, which could be especially valuable for initial screenings of materials with desired properties. Figure 4 shows that many bilayers are either metals (338 structures) or small gap semiconductors (about 100 structures). Besides, 49 bilayers have $E_g > 3$ eV, indicating that such nano-structured insulators make up a smaller portion in the pool of studied materials. The inclusion of SOC results in an overall decrease of E_g , however, the general trend of most materials being metals or small gap semiconductors is preserved, as seen in Fig. 4b. The band gap values are found to be consistent with the ones reported for 3D weakly bound layered solids¹⁵, where the majority of the materials are either metals or small gap semiconductors.

From the calculations we further show the correlation between the lattice parameters, average atomic numbers, and strength of SOC of the considered bilayers, given in the scattered plot in Fig. 4c for the ground states of the bilayers. Given that most topologically nontrivial materials have large SOC effects^{58,59}, the bilayers from our dataset with SOC > 0.4 eV maybe good candidates for further screening in terms of their topological characteristics.

Another important property for the interlayer interaction is the charge transfer that occurs upon bringing the two monolayers together. Using Bader charge analysis, here we calculate the charge difference Δq between the total charge of the individual monolayer (subscript ML) and the total charge of the monolayer as part of the bilayer structure (subscript sublayer in BL) using the relation,

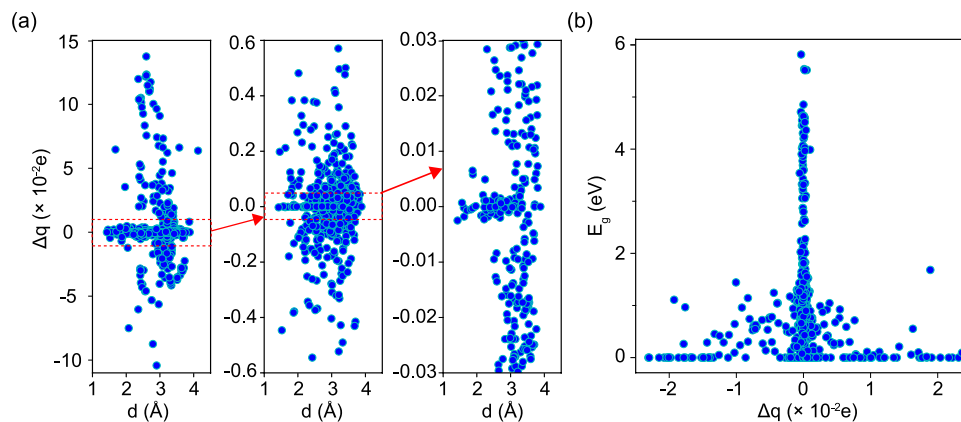


Fig. 5 (a) Charge difference Δq between an individual monolayer and the monolayer as part of the bilayer as a function of interlayer distances and (b) band gap E_g as a function of charge difference for the energetically most stable systems. The van der Waals correction is included in all calculations.

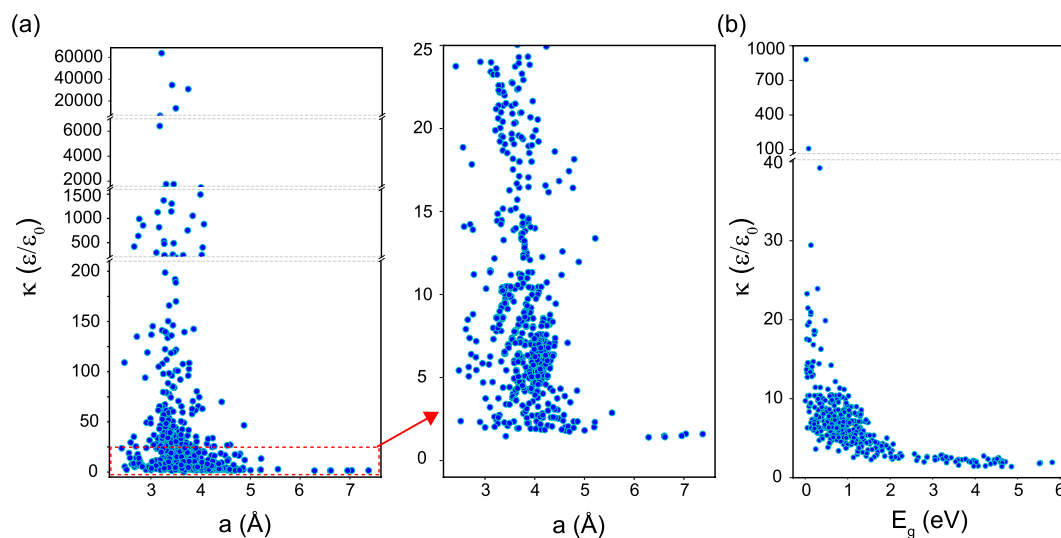


Fig. 6 Scattered plot of the dielectric constant scaled by the vacuum dielectric constant ϵ_0 as a function of the lattice constant (a) and and energy band gap (b) of the bilayer materials.

$$\Delta q = \sum_i^N [q_i M_i |_{ML} - q_i M_i |_{sublayer \text{ in } BL}], \quad (2)$$

where q_i is the charge of i -th atom (M_i) and the summation runs over the total number of atomic species in each monolayer class. This is a quantitative measure of the charge redistribution occurring in the bilayer formation as the monolayers are brought together. Data for Δq as a function of the interlayer separation is given in Fig. 5a as a scattered plot for the energetically most stable bilayers. The negative and positive spreads of Δq in Fig. 5a show charge transfer that occurs to and from the monolayer upon forming the bilayer. The results suggest that for the majority of materials, the charge transfer is rather small lying in the $-0.5 \times 10^{-2}e < \Delta q < 0.5 \times 10^{-2}e$ range. This is consistent with a weaker interlayer coupling, also discussed earlier in the context of the interlayer separation. Further information can be obtained from the E_g vs Δq correlation displayed in Fig. 5b. It is found that there is a Gaussian-like spread of the gap with Δq for bilayers with $E_g \neq 0$, while in metallic systems charge transfer occurs in the entire studied range.

The dielectric constant κ is also calculated within DFT, and results for κ as a function of the lattice constant are shown in Fig. 6a. The zoom-in view of the $\kappa < 25$ window shows the distribution of the data for bilayers with smaller dielectric constant. It is found that about 541 bilayers have $\kappa < 25$, while 60 systems have $\kappa > 100$. Figure 6b further shows the dielectric constant vs the energy band gap of the bilayers in their ground state. This data may be useful for the search of “high- κ ” and/or large gap dielectric nano-structured materials for the next generation electronic devices^{60,61}. In addition to large κ responsible for enhanced capacitive coupling, dielectrics with a large band gap are needed to prevent leakage currents between electrodes for successful integration.

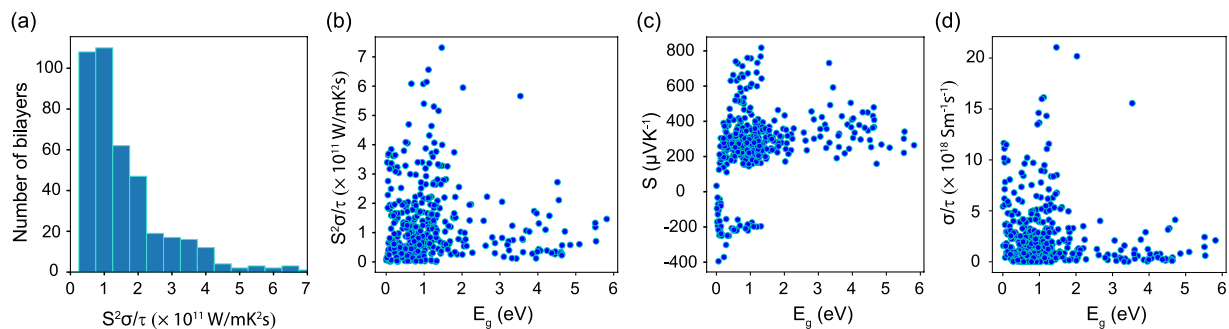


Fig. 7 (a) Histogram plot for the number of materials and their power factors ($S^2\sigma/\tau$), (b) the power factor $S^2\sigma/\tau$ as a function of E_g for bilayers with non-zero band gap at chemical potential $\mu=0$ and $T=300$ K, (c) the Seebeck coefficient S , and (d) conductivity (σ/τ) as a function of E_g for bilayers with non-zero band gap at chemical potential $\mu=0$ and $T=300$ K.

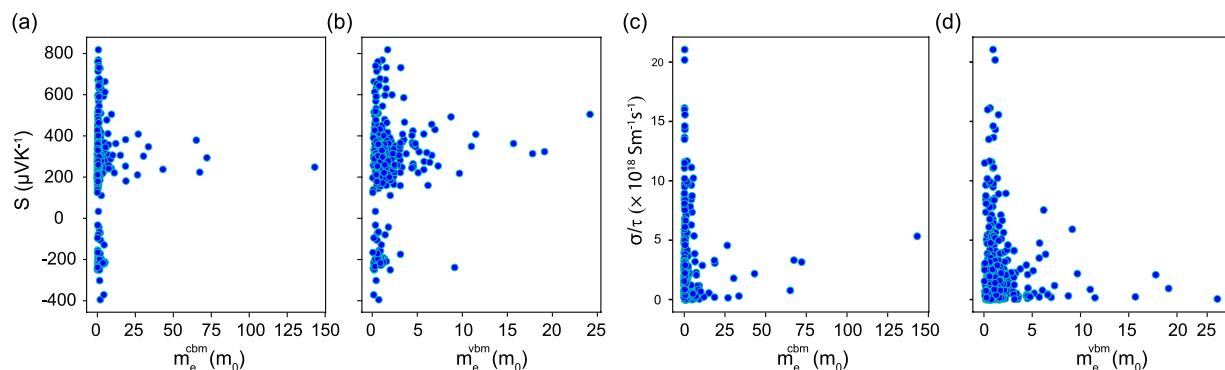


Fig. 8 Scattered plot of Seebeck coefficient vs: (a) the effective mass at the conduction band minimum; (b) the effective mass at the valence band maximum. Scattered plot of the scaled by the constant relaxation time electrical conductivity vs: (a) the effective mass at the conduction band minimum; (b) the effective mass at the valence band maximum. All masses are given in terms of the electron rest mass m_0 . The reported data correspond to zero chemical potential and 300 K temperature.

Transport calculations. Transport properties such as electrical conductivity, Seebeck coefficient, and power factor are widely used for evaluating the materials thermoelectric figure of merit $ZT = S^2\sigma T/\kappa_{th}$, where S , σ , T , and κ_{th} are the Seebeck coefficient, electrical conductivity, temperature, and thermal conductivity, respectively. Materials with higher ZT are sought out for efficient thermoelectric devices. One way to achieve this goal is to look for materials with large values of their power factors $S^2\sigma$. Using the semi-classical linearized Boltzmann transport theory within the constant relaxation time (τ) approximation (τ is material dependent and it typically requires separate experimental and theoretical studies) as implemented in the BoltzTraP2 code⁶², we have calculated S , σ , and $S^2\sigma$ for the energetically most stable bilayers. The simulations are performed with 3240 k -points, which is a dense enough mesh to obtain the transport properties.

After calculating S and σ/τ , we obtain the rescaled by the relaxation time power factor. A histogram plot distribution of $S^2\sigma/\tau$ for the number of considered bilayers is shown in Fig. 7a. The correlation between the power factor correlates and the band gap of the bilayers is also shown in Fig. 7b. The bilayers with large power factors may be a starting point to search for materials with improved thermoelectric properties at the nanoscale. The effective mass associated with each electronic structure is an important descriptor for the materials power factors and figures of merit as reported in high throughput calculations for bulk materials (mostly binary structures)^{63,64}. These quantities are readily available from DFT calculations, which can help one to assess if a given material may be a potential thermoelectric candidate. In Fig. 8, we give S and σ/τ values for bilayers with nonzero E_g . One observes that largest σ/τ and S values are found for materials with smaller m_e and m_h , which correlates well with data for 3D bulk materials^{63,64}.

Data Records

Our BMDS dataset containing 760 bilayer materials are composed of identical dynamically stable and nonmagnetic monolayers from the C2DB. The reported data contains information for the ground state stacking order of each material. All calculated data for the ground state bilayers are given in a CSV spreadsheet file and it can be found on figshare⁴³. The figures for the electronic band structure with considering relativistic SOC effect and the transport coefficients at different temperature with varying the chemical potential are also provided in figshare. The description of the columns in the spreadsheet are shown explicitly the Table 1. We have provided

Columns names	Type	Unit	Descriptions
materials	string	None	Monolayer materials name and id from C2DB database
bilayer_materials	string	None	Our BMDS bilayer materials name and its id
ground_state_stacking	string	None	Energetically most stable bilayer stacking configuration
a_mono	float	Å	Lattice parameters of monolayers
a	float	Å	Lattice parameter <i>a</i> of relaxed ground state stacking bilayer
b	float	Å	Lattice parameter <i>b</i> of relaxed ground state stacking bilayer
DFT_energy_bi	float	eV	DFT energy of relaxed ground state stacking bilayer
magnetic_moment	float	μ_B	Magnetic moment of each bilayer
formation_energy	float	eV/atom	Formation energies of bilayers
area	float	Å ²	Surface area of unit cell of relaxed ground state stacking bilayer
d	float	Å	Interlayer distance of relaxed ground state stacking bilayer
space_group	string	None	Space group of relaxed ground state stacking bilayer
no_soc_bandgap	float	eV	Band gap of relaxed ground state stacking bilayer without SOC
soc_bandgap	float	eV	Band gap of relaxed ground state stacking bilayer with SOC
dielectric_constant	float	None	Static dielectric constant of relaxed ground state stacking bilayer
soc_energy	float	eV/atom	SOC energy per atom
del_e_bilayer_bottom_and_mono	float	e	Charge transfer from bottom layer of bilayer
PF_xx	float	W/mK ² s	Power factor along in-plane direction
PF_zz	float	W/mK ² s	Power factor along out of plane direction
S_xx	float	μ VK ⁻¹	Seebeck coefficient along in-plane direction
S_zz	float	μ VK ⁻¹	Seebeck coefficient along out of plane direction
σ_{xx}	float	S m ⁻¹ s ⁻¹	Conductivity along in-plane direction
σ_{zz}	float	S m ⁻¹ s ⁻¹	Conductivity along out of plane direction
effective_mass_CBM	float	m_0	Effective mass at conduction band minimum
effective_mass_VBM	float	m_0	Effective mass at valence band maximum

Table 1. Detailed description of column names in the CSV spreadsheet containing the BMDS dataset. All properties are calculated for relaxed stable stacking bilayers.

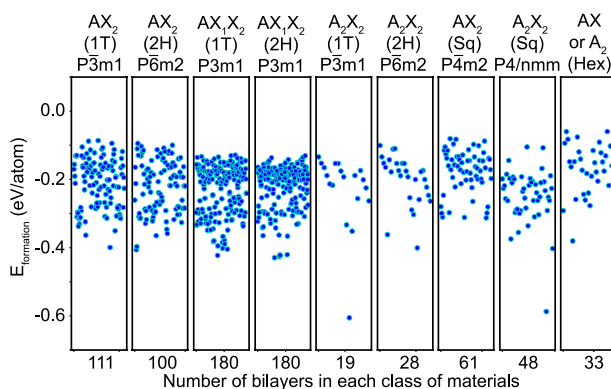


Fig. 9 Scattered plot of the formation energy for the most stable configuration as a function of number bilayer materials in each bilayer class. Negative $E_{\text{formation}}$ is indicative of the structural stability of the bilayers.

two columns labeled as “materials” and “bilayer_materials” in the CSV file, which correspond to the monolayer material name id from C2DB and our BMDS bilayer materials name and its id, respectively. We have included lattice constants of monolayers and bilayers, interlayer distances, DFT total energies, binding energies, unit cell surface areas, space groups, band gaps with and without considering the SOC effect, dielectric constants, SOC energies, and charge transfer (taking the bottom layer as a reference) data in the CSV file.

Transport properties, such as a Seebeck coefficient, power factor, and conductivity at $T = 300$ K and $\mu = 0$ for insulating bilayers are also reported in the CSV file. Additionally, effective masses at the VBM and CBM for insulating materials are included in the CSV file. Transport properties and effective masses of VBM and CBM are obtained for bilayers with nonzero energy gap. For metallic systems, that block is denoted as “metal”. Note that we considered all reported dynamically stable and nonmagnetic C2DB monolayers, however, some bilayers did not attain a stable interlayer separation, which became quite large or very small during the relaxation process (>8 Å or <1 Å in most cases). Such bilayers are discarded and the reported 760 bilayers are well converged structures. Also, while we considered only nonmagnetic monolayers, 24 bilayers acquired finite magnetic moments ($>0.5 \mu_B$). Therefore we have added a column for magnetic moment in the CSV file. For these magnetic bilayers,

Bilayer materials and id	d (Å) (BMDs)	d (Å) (previously reported)	E _g (eV) (BMDs)	E _g (eV) (previously reported)	Stacking
SeHfS-SeHfS	3.086	2.802	0.715	0.415	AA (a) ⁷⁹
SeHfS-SHfSe	3.086	2.8	0.703	0.426	AA1 (a) ⁷⁹
SHfSe-SeHfS	3.219	2.868	0.736	0.736	AA1 (a) ⁷⁹
TeMoSe-TeMoSe	3.384	3.19	0.836	0.562	AB (b) ³³
SeMoS-SeMoS	3.153	3.12	0.9419	0.96	AA2 (a) ^{80,81}
TeMoS-TeMoS	3.153	3.018	0.1246	0	AA2 (a) ³³
SeWS-SeWS	3.197	—	1.1573	1	AB (a) ⁸²
TeMoSe-SeMoTe	3.093	3.01	0.6275	0.46	AA2 (a) ³³
SeMoS-SMoSe	3.022	2.831	0.9418	0.81	AA2 (a) ⁸¹
SeWS-SWSe	3.048	—	1.1566	1.0	AA2 (a) ⁸²
SeMoTe-TeMoSe	3.436	3.289	1.0617	1.001	AB (b) ³³
SMoSe-SeMoS	3.348	3.2	1.3295	1.23	AB (a) ⁸³
SWSe-SeWS	3.254	—	1.2952	1.3	AB (a) ⁸²
HfSe ₂ -HfSe ₂	3.114	2.96	0.5143	1.07	AA (a) ⁶⁵
PtS ₂ -PtS ₂	2.253	2.54	0.7483	0.99	AA (a) ⁸⁴
PtSe ₂ -PtSe ₂	2.274	2.14	0.1876	0.19	AA (a) ⁸⁵
PtTe ₂ -PtTe ₂	2.40	2.39	0	0	AA (a) ⁸⁶
SnS ₂ -SnS ₂	3.029	2.95	1.51	1.53	AA (a) ⁴⁹
ZrS ₂ -ZrS ₂	2.987	—	1.079	1.09	AA (a) ⁸⁷
ZrSe ₂ -ZrSe ₂	3.095	3.08	0.3796	0.99	AA (a) ⁶⁵
MoS ₂ -MoS ₂	3.072	—	1.31	1.24	AB (a) ^{88,89}
MoSe ₂ -MoSe ₂	3.206	—	1.215	1.2	AB (a) ^{88,89}
MoTe ₂ -MoTe ₂	3.427	3.41	0.980	0.98	AB (a) ^{89,90}
NbSe ₂ -NbSe ₂	2.939	3.042	0	0	AB1 (a) ⁹¹
WO ₂ -WO ₂	2.547	—	1.2	1.22	AA2 (a) ⁸⁹
WS ₂ -WS ₂	3.161	—	1.507	1.43	AB (a) ⁸⁹
WSe ₂ -WSe ₂	3.218	—	1.389	1.23	AB (a) ⁸⁹
WTe ₂ -WTe ₂	3.43	—	1.024	0.99	AB (a) ⁸⁹
BN-BN	3.453	3.34	4.517	4.56	AA1 (a) ⁹²
GaN-GaN	2.330	2.47	2.02	2.01	AA1 (a) ⁹³
As ₂ -As ₂	3.270	3.270	0.920	0.7	AA (a) ⁹⁴
C ₂ -C ₂	3.493	3.46	0	0	AB (a) ⁹⁵

Table 2. A comparison of interlayer distances, band gaps, and stacking patterns of several bilayers in the BMDs dataset with results reported in other references. The stacking pattern notation is used as per the BMDs conventions. The label a (b) denotes bilayers whose stacking pattern for the energetically most stable configuration obtained here and by others is the same (different). In some cases, values for *d* and/or *E_g* are not reported.

we have reported the spin polarized calculations. We find that all magnetic bilayers are metallic, thus their transport properties are not evaluated.

Technical Validation

For the bilayer dataset presented here, we have taken electronically and dynamically stable nonmagnetic monolayers from the well known C2DB database (<https://cmrdb.fysik.dtu.dk/c2db/cmrdb-c2db>). First principles calculations are done using DFT methods with included van der Waals interactions. Such an approach is extensively used by the solid state physics and chemistry communities for materials predictions and property investigations. VASP is a premier quantum mechanical software package through which many emerging databases (including C2DB) are built. Each step of our high throughput calculations is checked with stringent convergence criteria. The stacking order of each bilayer is generated by utilizing previously established symmetry based criteria capturing the energetically most stable pattern configurations as reported by numerous references^{44–50}.

The vast majority of bilayer materials in BMDs have not been studied before. Therefore, we examine their stability by calculating the bilayer formation energy as: $E_{\text{formation}} = E_{\text{bilayer}} - 2 \times E_{\text{monolayer}}$, where $E_{\text{monolayer}}$ and E_{bilayer} are the total energies of monolayer and its corresponding ground state stacked bilayer structures, respectively. Normally, negative formation energy values indicate structural stability of the bilayer. Figure 9 shows $E_{\text{formation}}$ for the studied materials. All bilayers are found to have negative formation energies, such that $-0.7 \text{ eV/atom} < E_{\text{formation}} < 0 \text{ eV/atom}$. The only exception is the bilayer MgCl_2 in the square AX_2 phase, for which $E_{\text{formation}} = 1.24 \text{ eV/atom}$ and it is not explicitly given in Fig. 9. We also note that all individual monolayers in our bilayer dataset are reported as dynamically stable in the C2DB database^{16,42} due to the lack of negative phonon modes. Additionally, several studies have shown that many bilayers composed of monolayers from the AX_2 , AX_1X_2 , AX and A_2 classes also have phonon band structure lacking negative modes^{65–72} demonstrating a

dynamical stability for stacking patterns considered here as well. Although the phonon dispersion is an important factor for the stability of materials, it requires careful examination in terms of type and size of the constructed supercells, different functionals, and/or smearing parameters^{73–77}. While small differences in bond lengths and angles may not show noticeable differences in the electronic structure, they are detrimental for the phonon band structure. Changes in the interlayer separation, which is closely related to the particular vdW dispersion method, can also have important consequences for the presence or lack of negative phonons of layered materials. We note that the monolayers dynamical stability and the several studies on vdW bilayers are strong indicators for the stability of the bilayer dataset here. The crucial influence of the specific DFT approximations and parameters on the phonon dispersion is materials dependent, thus phonon calculations are not part of this high throughput study.

The electronic structure properties of several bilayers have also been studied computationally by others. A comparison of the interlayer distances, band gaps, and stacking patterns of previously reported and calculated here data are shown in Table 2. Most of the stacking patterns are identical to our results (indicated with (a) label), with the exception of what was reported for the Janus bilayers made of TeMoSe and SeMoTe monolayers (indicated with a (b) label), mainly due to the more stringent relaxation convergence criteria used in our simulations. Table 2 further shows that there are greater dissimilarities in some band gaps (although good agreement is found for many cases). The main reason is that a variety of exchange–correlation functionals and van der Waals interaction approximations are considered by the different authors. Nevertheless, there is generally a good agreement for the interlayer distances, especially for most transition metal dichalcogenides⁷⁸ for which $d = 3\text{--}3.5\text{ Å}$ are found.

Usage Notes

The data for the bilayers BMDs can be accessed directly from the CSV spreadsheet provided in figshare⁴³. The dataset can further be expanded by considering bilayers formed of other 2D monolayers with different lattice structures which may or may not host magnetic states.

Code availability

In addition to the CSV file, several components to work with the reported bilayer materials can be found in figshare⁴³ and in GitHub (<https://github.com/rkb12/BMDB-database>).

In the stacking-pattern-PYTHON-code-for-each-class zipped directory, a code that obtains all possible stacking patterns (following the naming notation in Fig. 2) are given. Inside each subdirectory, a prototype example of monolayer structure and the corresponding stacking code are given. Executing the code in the same directory will create the stacking patterns for the respective class of bilayer.

In the zipped soc-bandstructure-code, an in-house code generating the band structure with SOC is provided. The code reads a VASP output file and generates a graphical representation for the band structure.

In the zipped transport-cal-code, an in-house code generating the transport properties such as conductivity (σ/τ), Seebeck coefficient (S), and power factor ($S^2\sigma/\tau$) as function of chemical potential at different temperature for each bilayer material. The code reads VASP and BoltzTraP output files and generates a graphical representation for the transport properties.

In the zipped soc-bandstructure-figures and transport-figures a graphical representation for the energy band structure (with and without SOC) and transport properties for the ground state stacking compositions of all bilayer materials are also given.

Received: 16 January 2023; Accepted: 11 April 2023;

Published online: 21 April 2023

References

1. Thi-Xuan Dang, D., Barik, R. K., Phan, M.-H. & Woods, L. M. Enhanced Magnetism in Heterostructures with Transition-Metal Dichalcogenide Monolayers. *J. Phys. Chem. Lett.* **13**, 8879–8887, <https://doi.org/10.1021/acs.jpclett.2c01925> (2022).
2. Marjaoui, A., Tamer, M. A., El Kasmi, A., Diani, M. & Zanouni, M. First-principles Study on Electronic and Thermoelectric Properties of Janus Monolayers AsXC₃ (X: Sb, Bi). *Comput. Condens. Matter* e00623, <https://doi.org/10.1016/j.cocom.2021.e00623> (2021).
3. Kim, H., Anasori, B., Gogotsi, Y. & Alshareef, H. N. Thermoelectric Properties of Two-dimensional Molybdenum-based MXenes. *Chem. Mater.* **29**, 6472–6479, <https://doi.org/10.1021/acs.chemmater.7b02056> (2017).
4. Sharma, V., Kagdada, H. L., Jha, P. K., Śpiwak, P. & Kurzydłowski, K. J. Thermal Transport Properties of Boron Nitride Based Materials: A Review. *Renew. Sust. Energ. Rev.* **120**, 109622, <https://doi.org/10.1016/j.rser.2019.109622> (2020).
5. Lv, H., Lu, W., Shao, D. & Sun, Y. Enhanced Thermoelectric Performance of Phosphorene by Strain-induced Band Convergence. *Phys. Rev. B* **90**, 085433, <https://doi.org/10.1103/PhysRevB.90.085433> (2014).
6. Kaur, K., Khandy, S. A., Dhiman, S., Sharopov, U. & Singh, J. Computational Prediction of Thermoelectric Properties of 2D Materials. *Electronic Structure* <https://doi.org/10.1088/2516-1075/ac635b> (2022).
7. Li, D. *et al.* Recent Progress of Two-dimensional Thermoelectric Materials. *Nano-Micro Lett.* **12**, 1–40, <https://doi.org/10.1007/s40820-020-0374-x> (2020).
8. Cheng, J., Wang, C., Zou, X. & Liao, L. Recent Advances in Optoelectronic Devices Based on 2D Materials and Their Heterostructures. *Adv. Opt. Mater.* **7**, 1800441, <https://doi.org/10.1002/adom.201800441> (2019).
9. Hu, G. & Xiang, B. Recent Advances in Two-dimensional Spintronics. *Nanoscale Res. Lett.* **15**, 1–17, <https://doi.org/10.1186/s11671-020-03458-y> (2020).
10. Novoselov, K. S. *et al.* Electric Field Effect in Atomically Thin Carbon Films. *Science* **306**, 666–669, <https://doi.org/10.1126/science.1102896> (2004).
11. Barik, R. K. & Singh, A. K. Accelerated Discovery of the Valley-Polarized Quantum Anomalous Hall Effect in MXenes. *Chem. Mater.* **33**, 6311–6317, <https://doi.org/10.1021/acs.chemmater.1c00798> (2021).
12. Cao, T. *et al.* Valley-selective Circular Dichroism of Monolayer Molybdenum Disulphide. *Nat. Commun.* **3**, 1–5, <https://doi.org/10.1038/ncomms1882> (2012).

13. Wu, K. *et al.* Two-dimensional Giant Tunable Rashba Semiconductors with Two-atom-thick Buckled Honeycomb Structure. *Nano Lett.* **21**, 740–746, <https://doi.org/10.1021/acs.nanolett.0c04429> (2020).
14. Hastrup, S. *et al.* The Computational 2D Materials Database: High-throughput Modeling and Discovery of Atomically Thin Crystals. *2d Mater.* **5**, 042002, <https://doi.org/10.1088/2053-1583/aacfc1> (2018).
15. Cheon, G. *et al.* Data Mining for New Two- and One-dimensional Weakly Bonded Solids and Lattice-commensurate Heterostructures. *Nano Lett.* **17**, 1915–1923, <https://doi.org/10.1021/acs.nanolett.6b05229> (2017).
16. Gjerding, M. N. *et al.* Recent Progress of the Computational 2D Materials Database (C2DB). *2d Mater.* **8**, 044002, <https://doi.org/10.1088/2053-1583/ac1059> (2021).
17. Lv, R. *et al.* Transition Metal Dichalcogenides and Beyond: Synthesis, Properties, and Applications of Single- and Few-layer Nanosheets. *Acc. Chem. Res.* **48**, 56–64, <https://doi.org/10.1021/ar5002846> (2015).
18. Kim, K. K. *et al.* Synthesis of Monolayer Hexagonal Boron Nitride on Cu Foil using Chemical Vapor Deposition. *Nano Lett.* **12**, 161–166, <https://doi.org/10.1021/nl203249a> (2012).
19. Hawaldar, R. *et al.* Large-area High-throughput Synthesis of Monolayer Graphene Sheet by Hot Filament Thermal Chemical Vapor Deposition. *Sci. Rep.* **2**, 1–9, <https://doi.org/10.1038/srep00682> (2012).
20. Sargar, A., Patil, N., Mane, S., Gawale, S. & Bhosale, P. Electrochemical Synthesis and Characterisation of ZrSe₂ Thin Films. *Int. J. Electrochem. Sci.* **4**, 87–894, <http://www.electrochemsci.org/papers/vol4/4060887.pdf> (2009).
21. Yue, R. *et al.* HfSe₂ Thin Films: 2D Transition Metal Dichalcogenides Grown by Molecular Beam Epitaxy. *ACS nano* **9**, 474–480, <https://doi.org/10.1021/nn5056496> (2015).
22. Zhang, M. *et al.* Controlled Synthesis of ZrS₂ Monolayer and Few Layers on Hexagonal Boron Nitride. *J. Am. Chem. Soc.* **137**, 7051–7054, <https://doi.org/10.1021/jacs.5b03807> (2015).
23. Biener, M. M., Biener, J. & Friend, C. M. Novel Synthesis of Two-dimensional TiS₂ Nanocrystallites on Au (111). *J. Chem. Phys.* **122**, 034706, <https://doi.org/10.1063/1.1826054> (2005).
24. Zhang, J. *et al.* Janus Monolayer Transition-metal Dichalcogenides. *ACS nano* **11**, 8192–8198, <https://doi.org/10.1021/acsnano.7b03186> (2017).
25. Wickramaratne, D., Zahid, F. & Lake, R. K. Electronic and Thermoelectric Properties of Van der Waals Materials with Ring-shaped Valence Bands. *J. Appl. Phys.* **118**, 075101, <https://doi.org/10.1063/1.4928559> (2015).
26. Fan, Q., Zhang, W., Qing, H. & Yang, J. Exceptional Thermoelectric Properties of Bilayer GeSe: First Principles Calculation. *Materials* **15**, 971, <https://doi.org/10.3390/ma15030971> (2022).
27. Castro, E. V. *et al.* Biased Bilayer Graphene: Semiconductor with a Gap Tunable by the Electric Field Effect. *Phys. Rev. Lett.* **99**, 216802, <https://doi.org/10.1103/PhysRevLett.99.216802> (2007).
28. Liu, X., Pyatakov, A. P. & Ren, W. Magnetoelectric Coupling in Multiferroic Bilayer VS₂. *Physical Review Letters* **125**, 247601, <https://doi.org/10.1103/PhysRevLett.125.247601> (2020).
29. Wang, Y. *et al.* Stacking-dependent Optical Conductivity of Bilayer Graphene. *ACS Nano* **4**, 4074–4080, <https://doi.org/10.1021/nn1004974> (2010).
30. Li, Z. *et al.* Stacking-dependent exciton multiplicity in wse₂ bilayers. *Phys. Rev. B* **106**, 045411, <https://doi.org/10.1103/PhysRevB.106.045411> (2022).
31. Popescu, A., Rodriguez-Lopez, P. & Woods, L. M. Composition and Stacking Dependent Topology in Bilayers from the Graphene Family. *Phys. Rev. Mater.* **3**, 064002, <https://doi.org/10.1103/PhysRevMaterials.3.064002> (2019).
32. Sivadas, N., Okamoto, S., Xu, X., Fennie, C. J. & Xiao, D. Stacking-dependent Magnetism in Bilayer CrI₃. *Nano Lett.* **18**, 7658–7664, <https://doi.org/10.1021/acs.nanolett.8b03321> (2018).
33. Rezavand, A. & Ghobadi, N. Stacking-dependent Rashba Spin-splitting in Janus Bilayer Transition Metal Dichalcogenides: The Role of In-plane Strain and Out-of-plane Electric Field. *Phys. E: Low-Dimens. Syst. Nanostructures*. **132**, 114768, <https://doi.org/10.1016/j.physe.2021.114768> (2021).
34. Po, H. C., Zou, L., Vishwanath, A. & Senthil, T. Origin of Mott Insulating Behavior and Superconductivity in Twisted Bilayer Graphene. *Phys. Rev. X* **8**, 031089, <https://doi.org/10.1103/PhysRevX.8.031089> (2018).
35. Kezilebieke, S. *et al.* Moiré-enabled Topological Superconductivity. *Nano Lett.* **22**, 328–333, <https://doi.org/10.1021/acs.nanolett.1c03856> (2022).
36. Zhu, Y. *et al.* Tunable Multi-bands in Twisted Double Bilayer Graphene. *2D Mater.* **9**, 034001, <https://doi.org/10.1088/2053-1583/ac69bb> (2022).
37. Rodriguez-Lopez, P., Le, D.-N., Caldera³n, M. J., Bascones, E. & Woods, L. M. Twisted Bilayered Graphenes at Magic Angles and Casimir Interactions: Correlation-driven Effects. *2D Mater.* **10**, 014006, <https://doi.org/10.1088/2053-1583/ac97f2> (2022).
38. Zhao, P. *et al.* Equilibrium Chemical Vapor Deposition Growth of Bernal-stacked Bilayer Graphene. *ACS Nano* **8**, 11631–11638, <https://doi.org/10.1021/nn5049188> (2014).
39. Yao, M. *et al.* Materials Informatics Platform with Three Dimensional Structures, Workflow and Thermoelectric Applications. *Sci. Data* **8**, 1–10, <https://doi.org/10.1038/s41597-021-01022-6> (2021).
40. Khatavkar, N., Swetlana, S. & Singh, A. K. Accelerated Prediction of Vickers Hardness of Co- and Ni-based Superalloys from Microstructure and Composition using Advanced Image Processing Techniques and Machine Learning. *Acta Mater.* **196**, 295–303, <https://doi.org/10.1016/j.actamat.2020.06.042> (2020).
41. Swetlana, S., Khatavkar, N. & Singh, A. K. Development of Vickers Hardness Prediction Models via Microstructural Analysis and Machine Learning. *J. Mater. Sci.* **55**, 15845–15856, <https://doi.org/10.1007/s10853-020-05153-w> (2020).
42. Thygesen, K. S. *Computational 2D Materials Database (C2DB)* <https://doi.org/10.11583/DTU.14616660> (2021).
43. Barik, R. K. & Woods, L. M. High Throughput Calculations of Bilayer Materials: BMDB Database. *Figshare* <https://doi.org/10.6084/m9.figshare.21799475> (2022).
44. Wang, S. *et al.* Stacking-Engineered Heterostructures in Transition Metal Dichalcogenides. *Adv. Mater.* **33**, 2005735, <https://doi.org/10.1002/adma.202005735> (2021).
45. Pandey, S. K., Das, R. & Mahadevan, P. Layer-dependent Electronic Structure Changes in Transition Metal Dichalcogenides: the Microscopic Origin. *ACS Omega* **5**, 15169–15176, <https://doi.org/10.1021/acsomega.0c01138> (2020).
46. Naik, M. H., Maity, I., Maiti, P. K. & Jain, M. Kolmogorov-Crespi Potential for Multilayer Transition-metal Dichalcogenides: Capturing Structural Transformations in Moiré Superlattices. *J. Phys. Chem. C* **123**, 9770–9778, <https://doi.org/10.1021/acs.jpcc.8b10392> (2019).
47. Augustin Lu, A. K., Yayama, T., Morishita, T., Spencer, M. J. & Nakanishi, T. Uncovering New Buckled Structures of Bilayer GaN: A First-Principles Study. *J. Phys. Chem. C* **123**, 1939–1947, <https://doi.org/10.1021/acs.jpcc.8b09973> (2018).
48. Chen, E., Xu, W., Chen, J. & Warner, J. 2D Layered Noble Metal Dichalcogenides (Pt, Pd, Se, S) for Electronics and Energy Applications. *Mater. Today Adv.* **7**, 100076, <https://doi.org/10.1016/j.mtaadv.2020.100076> (2020).
49. Bacaksiz, C. *et al.* Bilayer SnS₂: Tunable Stacking Sequence by Charging and Loading Pressure. *Phys. Rev. B* **93**, 125403, <https://doi.org/10.1103/PhysRevB.93.125403> (2016).
50. Zhang, L., Zhang, X. & Lu, G. Predictions of Moiré Excitons in Twisted Two-dimensional Organic-inorganic Halide Perovskites. *Chem. Sci.* **12**, 6073–6080, <https://doi.org/10.1039/D1SC00359C> (2021).
51. Kresse, G. & Hafner, J. Ab Initio Molecular Dynamics for Liquid Metals. *Phys. Rev. B* **47**, 558–561, <https://doi.org/10.1103/PhysRevB.47.558> (1993).

52. Kresse, G. & Joubert, D. From Ultrasoft Pseudopotentials to the Projector Augmented-wave Method. *Phys. Rev. B* **59**, 1758–1775, <https://doi.org/10.1103/PhysRevB.59.1758> (1999).
53. Perdew, J. P., Burke, K. & Ernzerhof, M. Generalized Gradient Approximation Made Simple. *Phys. Rev. Lett.* **77**, 3865–3868, <https://doi.org/10.1103/PhysRevLett.77.3865> (1996).
54. Monkhorst, H. J. & Pack, J. D. Special Points for Brillouin-zone Integrations. *Phys. Rev. B* **13**, 5188–5192, <https://doi.org/10.1103/PhysRevB.13.5188> (1976).
55. Tang, W., Sanville, E. & Henkelman, G. A Grid-based Bader Analysis Algorithm Without Lattice Bias. *J. Phys. Condens. Matter* **21**, 084204, <https://doi.org/10.1088/0953-8984/21/8/084204> (2009).
56. Grimme, S., Ehrlich, S. & Goerigk, L. Effect of the Damping Function in Dispersion Corrected Density Functional Theory. *J. Comput. Chem.* **32**, 1456–1465, <https://doi.org/10.1002/jcc.21759> (2011).
57. Ganose, A. M., Jackson, A. J. & Scanlon, D. O. Sumo: Command-line Tools for Plotting and Analysis of Periodic* Ab Initio* Calculations. *J. open source softw.* **3**, 717, <https://doi.org/10.21105/joss.00717> (2018).
58. Barik, R. K., Shinde, R. & Singh, A. K. Multiple Triple-point Fermions in Heusler Compounds. *J. Phys. Condens. Matter* **30**, 375702 (2018).
59. Barik, R. K., Kumar, R. & Singh, A. K. Topological Phases in Hydrogenated Group 13 Monolayers. *J. Phys. Chem. C* **123**, 25985–25990 (2019).
60. Ando, T. Ultimate Scaling of High- κ Gate Dielectrics: Higher- κ or Interfacial Layer Scavenging? *Materials* **5**, 478–500 (2012).
61. Wilk, G. D., Wallace, R. M. & Anthony, J. High- κ Gate Dielectrics: Current Status and Materials Properties Considerations. *J. Appl. Phys.* **89**, 5243–5275 (2001).
62. Madsen, G. K., Carrete, J. & Verstraete, M. J. BoltzTraP2, A Program for Interpolating Band Structures and Calculating Semi-classical Transport Coefficients. *Comput. Phys. Commun.* **231**, 140–145, <https://doi.org/10.1016/j.cpc.2018.05.010> (2018).
63. Yan, J. *et al.* Material Descriptors for Predicting Thermoelectric Performance. *Energy Environ. Sci.* **8**, 983–994, <https://doi.org/10.1039/C4EE03157A> (2015).
64. Suwardi, A. *et al.* Inertial Effective Mass as an Effective Descriptor for Thermoelectrics via Data-driven Evaluation. *J. Mater. Chem. A* **7**, 23762–23769, <https://doi.org/10.1039/C9TA05967A> (2019).
65. Yan, P., Gao, G.-y., Ding, G.-q. & Qin, D. Bilayer MSe₂ (M = Zr, Hf) as Promising Two-dimensional Thermoelectric Materials: a First-principles Study. *RSC Adv.* **9**, 12394–12403, <https://doi.org/10.1039/C9RA00586B> (2019).
66. Kandemir, A. & Sahin, H. Bilayers of Janus WSe: Monitoring the Stacking type via the Vibrational Spectrum. *Phys. Chem. Chem. Phys.* **20**, 17380–17386, <https://doi.org/10.1039/C8CP02802H> (2018).
67. Liu, J. & Zhang, W. Bilayer Silicene with an Electrically-tunable Wide Band Gap. *RSC Adv.* **3**, 21943–21948, <https://doi.org/10.1039/C3RA44392B> (2013).
68. Lamparski, M., Troeye, B. V. & Meunier, V. Soliton Signature in the Phonon Spectrum of Twisted Bilayer Graphene. *2d Mater.* **7**, 025050, <https://doi.org/10.1088/2053-1583/ab7874> (2020).
69. Bai, S. *et al.* Stacking Pattern Induced High ZTs in Monolayer SnS₂ and Bilayer SnXY (X/Y = S, Se) Materials with Strong Anharmonic Phonon Scattering. *Chem. Eng. J.* **455**, 140832, <https://doi.org/10.1016/j.cej.2022.140832> (2023).
70. Barhoumi, M., Lazaar, K., Bouzidi, S. & Said, M. A DFT Study of Janus Structure of S and Se in HfS₂ Layered as a Promising Candidate for Electronic Devices. *J. Mol. Graph. Model.* **96**, 107511, <https://doi.org/10.1016/j.jmgm.2019.107511> (2020).
71. Zhang, W., Yang, J.-Y. & Liu, L. Strong Interfacial Interactions Induced a Large Reduction in Lateral Thermal Conductivity of Transition-metal Dichalcogenide Superlattices. *RSC Adv.* **9**, 1387–1393, <https://doi.org/10.1039/C8RA10601K> (2019).
72. Goldstein, T. *et al.* Raman Scattering and Anomalous Stokes-anti-Stokes Ratio in MoTe₂ Atomic Layers. *Sci. Rep.* **6**, 1–7, <https://doi.org/10.1038/srep28024> (2016).
73. Pandey, S. C., Xu, X., Williamson, I., Nelson, E. B. & Li, L. Electronic and Vibrational Properties of Transition Metal-oxides: Comparison of GGA, GGA + U, and Hybrid Approaches. *Chem. Phys. Lett.* **669**, 1–8, <https://doi.org/10.1016/j.cplett.2016.12.005> (2017).
74. Ning, J., Furness, J. W. & Sun, J. Reliable Lattice Dynamics from an Efficient Density Functional Approximation. *Chem. Mater.* **34**, 2562–2568, <https://doi.org/10.1021/acs.chemmater.1c03222> (2022).
75. Kaczowski, J. & Plowaś-Korus, I. The Vibrational and Thermodynamic Properties of CsPbI₃ Polymorphs: an Improved Description based on the SCAN Meta-GGA Functional. *J. Phys. Chem. Lett.* **12**, 6613–6621, <https://doi.org/10.1021/acs.jpclett.1c01798> (2021).
76. Yan, J.-A., Cruz, M. A. D., Cook, B. & Varga, K. Structural, Electronic and Vibrational Properties of Few-layer 2H- and 1T-TaSe₂. *Sci. Rep.* **5**, 1–13, <https://doi.org/10.1038/srep16646> (2015).
77. Radescu, S., Machon, D. & Mélinon, P. Origin of dynamical instabilities in some simulated two-dimensional materials: Gase as a case study. *Phys. Rev. Mater.* **3**, 074002, <https://doi.org/10.1103/PhysRevMaterials.3.074002> (2019).
78. Wang, Z., Li, R., Su, C. & Loh, K. P. Intercalated Phases of Transition Metal Dichalcogenides. *SmartMat* **1**, e1013, <https://doi.org/10.1002/smm2.1013> (2020).
79. Ghobadi, N. & Touski, S. B. The Electrical and Spin Properties of Monolayer and Bilayer Janus HfS₂ under Vertical Electrical Field. *J. Phys. Condens. Matter* **33**, 085502, <https://doi.org/10.1088/1361-648X/abcb12> (2020).
80. Wei, S., Li, J., Liao, X., Jin, H. & Wei, Y. Investigation of Stacking Effects of Bilayer MoS₂ on Photocatalytic Water Splitting. *J. Phys. Chem. C* **123**, 22570–22577, <https://doi.org/10.1021/acs.jpcc.9b04784> (2019).
81. Yin, W.-J., Wen, B., Nie, G.-Z., Wei, X.-L. & Liu, L.-M. Tunable Dipole and Carrier Mobility for a Few Layer Janus MoS₂ Structure. *J. Mater. Chem. C* **6**, 1693–1700, <https://doi.org/10.1039/C7TC05225A> (2018).
82. Guo, J., Ke, C., Wu, Y. & Kang, J. Strain Engineering on the Electronic and Optical Properties of WSe₂ Bilayer. *Nanoscale Res. Lett.* **15**, 1–9, <https://doi.org/10.1186/s11671-020-03330-z> (2020).
83. Shang, C. *et al.* Bandgap Tuning in MoS₂ Bilayers: Synergistic Effects of Dipole Moment and Interlayer Distance. *Phys. Chem. Chem. Phys.* **20**, 20919–20926, <https://doi.org/10.1039/C8CP04208J> (2018).
84. Zhao, Y. *et al.* Extraordinarily Strong Interlayer Interaction in 2D Layered PtS₂. *Adv. Mater.* **28**, 2399–2407, <https://doi.org/10.1002/adma.201504572> (2016).
85. Kandemir, A. *et al.* Structural, Electronic and Phononic Properties of PtSe₂: from Monolayer to Bulk. *Semicond. Sci. Technol.* **33**, 085002, <https://doi.org/10.1088/1361-6641/aacba2> (2018).
86. Li, J., Jin, H., Wei, Y. & Guo, H. Tunable Intrinsic Spin Hall Conductivity in Bilayer PtTe₂ by Controlling the Stacking Mode. *Phys. Rev. B* **103**, 125403, <https://doi.org/10.1103/PhysRevB.103.125403> (2021).
87. Shang, J., Huang, L. & Wei, Z. Effects of Vertical Electric Field and Compressive Strain on Electronic Properties of Bilayer ZrS₂. *J. Semicond.* **38**, 033001, <https://doi.org/10.1088/1674-4926/38/3/033001> (2017).
88. He, J., Hummer, K. & Franchini, C. Stacking Effects on the Electronic and Optical Properties of Bilayer Transition Metal Dichalcogenides MoS₂, MoSe₂, WS₂, and WSe₂. *Phys. Rev. B* **89**, 075409, <https://doi.org/10.1103/PhysRevB.89.075409> (2014).
89. Zeng, F., Zhang, W.-B. & Tang, B.-Y. Electronic Structures and Elastic Properties of Monolayer and Bilayer Transition Metal Dichalcogenides MX₂ (M = Mo, W; X = O, S, Se, Te): a Comparative First-principles Study. *Chin. Phys. B* **24**, 097103, <https://doi.org/10.1088/1674-1056/24/9/097103> (2015).
90. Lin, Z., Si, C., Duan, S., Wang, C. & Duan, W. Rashba Splitting in Bilayer Transition Metal Dichalcogenides Controlled by Electronic Ferroelectricity. *Phys. Rev. B* **100**, 155408, <https://doi.org/10.1103/PhysRevB.100.155408> (2019).
91. Lian, C.-S., Si, C., Wu, J. & Duan, W. First-principles Study of Na-intercalated Bilayer NbSe₂: Suppressed Charge-density Wave and Strain-enhanced Superconductivity. *Phys. Rev. B* **96**, 235426, <https://doi.org/10.1103/PhysRevB.96.235426> (2017).

92. Constantinescu, G., Kuc, A. & Heine, T. Stacking in Bulk and Bilayer Hexagonal Boron Nitride. *Phys. Rev. Lett.* **111**, 036104, <https://doi.org/10.1103/PhysRevLett.111.036104> (2013).
93. Xu, D., He, H., Pandey, R. & Karna, S. P. Stacking and Electric Field Effects in Atomically Thin Layers of GaN. *J. Phys. Condens. Matter* **25**, 345302, <https://doi.org/10.1088/0953-8984/25/34/345302> (2013).
94. Kecik, D., Durgun, E. & Ciraci, S. Optical Properties of Single-layer and Bilayer Arsenene Phases. *Phys. Rev. B* **94**, 205410, <https://doi.org/10.1103/PhysRevB.94.205410> (2016).
95. Fukaya, Y. *et al.* Atomic Arrangements of Quasicrystal Bilayer Graphene: Interlayer Distance Expansion. *Phys. Rev. B* **104**, L180202, <https://doi.org/10.1103/PhysRevB.104.L180202> (2021).

Acknowledgements

Financial support from the U.S. Department of Energy under grant no. DE-FG02-06ER46297. Computational resources are provided by USF Research Computing.

Author contributions

R.K.B. performed the calculations and L.M.W. conceived the idea, performed the analysis and wrote the paper. All authors reviewed the manuscript.

Competing interests

The authors declare no competing interests.

Additional information

Supplementary information The online version contains supplementary material available at <https://doi.org/10.1038/s41597-023-02146-7>.

Correspondence and requests for materials should be addressed to R.K.B. or L.M.W.

Reprints and permissions information is available at www.nature.com/reprints.

Publisher's note Springer Nature remains neutral with regard to jurisdictional claims in published maps and institutional affiliations.



Open Access This article is licensed under a Creative Commons Attribution 4.0 International License, which permits use, sharing, adaptation, distribution and reproduction in any medium or format, as long as you give appropriate credit to the original author(s) and the source, provide a link to the Creative Commons license, and indicate if changes were made. The images or other third party material in this article are included in the article's Creative Commons license, unless indicated otherwise in a credit line to the material. If material is not included in the article's Creative Commons license and your intended use is not permitted by statutory regulation or exceeds the permitted use, you will need to obtain permission directly from the copyright holder. To view a copy of this license, visit <http://creativecommons.org/licenses/by/4.0/>.

© The Author(s) 2023